Science Advances
AAAS

advances.sciencemag.org/cgi/content/full/6/4/eaay9851/DC1

Supplementary Materials for

Large-scale synthesis of crystalline g-C_3N_4 nanosheets and high-temperature H_2 sieving from assembled films

Luis Francisco Villalobos, Mohammad Tohidi Vahdat, Mostapha Dakhchoune, Zahra Nadizadeh, Mounir Mensi, Emad Oveisi, Davide Campi, Nicola Marzari, Kumar Varoon Agrawal*

*Corresponding author. Email: kumar.agrawal@epfl.ch

Published 24 January 2020, *Sci. Adv.* **6**, eaay9851 (2020)
DOI: 10.1126/sciadv.aay9851

This PDF file includes:

Fig. S1. XRD of layered PTI platelets.
Fig. S2. Bright-field TEM image of PTI crystals obtained after one synthesis cycle of 2 days.
Fig. S3. PTI crystal size evolution with synthesis time.
Fig. S4. PTI crystal size evolution with number of synthesis cycles.
Fig. S5. HRTEM of PTI platelets.
Fig. S6. Evolution of the exfoliation of PTI in anhydrous DMAc at 100°C.
Fig. S7. HRTEM images of a single-layer PTI nanosheet.
Fig. S8. HRTEM images of a few-layer PTI nanosheet.
Fig. S9. XPS spectra of PTI nanosheets.
Fig. S10. Interaction of methane molecule with PTI single-layer nanosheet.
Fig. S11. Fabrication of gas-sieving PTI films via vacuum filtration.
Fig. S12. Gas permeation data for PTI membranes.
Fig. S13. Mixed-gas performance of the PTI membranes with *m*-PBI chains as spacers between PTI nanosheets at 250°C.
Fig. S14. PES for H_2 on a PTI monolayer calculated using the NEB and the constrained relaxation methods.
Fig. S15. Diagram showing the selective layer of PTI membranes with *m*-PBI chains as spacers.
Table S1. Elemental analysis of PTI crystals using different synthesis conditions.
Table S2. Li and Cl content on PTI nanosheets.
Table S3. Performance of PTI nanosheet films incorporating *m*-PBI chains at different temperatures.
Supplementary Note I. Carbon nitride membranes fabricated using polymeric melon
Supplementary Note II. Ab initio simulation of interaction between CH_4 and a PTI nanosheet
Supplementary Note III. Calculation of activation energy
Supplementary Note IV. Availability of pores of PTI nanosheets for transport of molecules
Supplementary Note V. Use of *m*-PBI chains as spacers

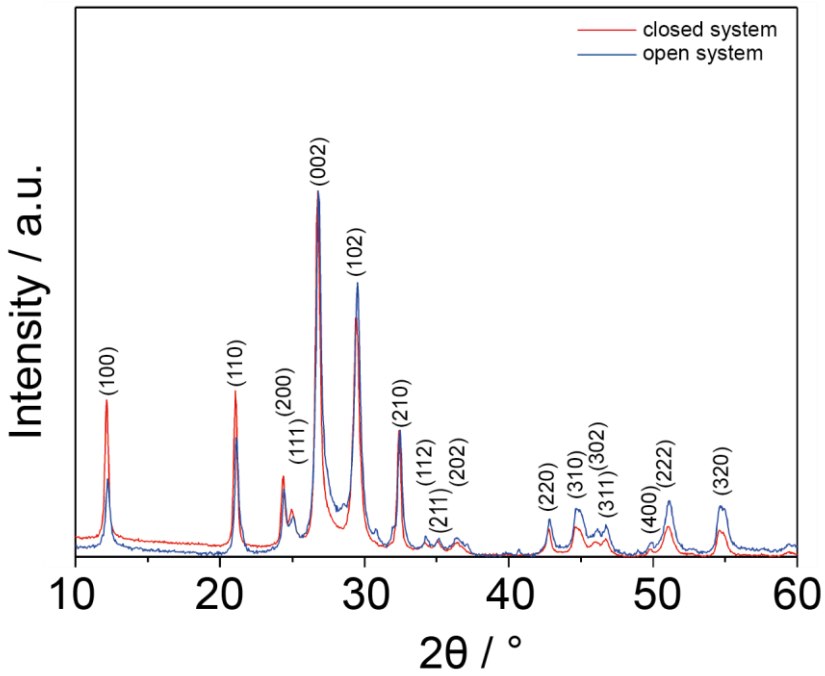

Fig. S1. XRD of layered PTI platelets. Powder XRD pattern of crystalline PTI synthesized in a closed system (i.e., quartz ampule under vacuum) as reported originally by Wirnhier et al.(*16*), and synthesized using the open system approach presented in this work. For the open system case, PTI from a large batch of 5.8 g of PTI was used for the measurement. The XRD measurements were done using the same conditions.

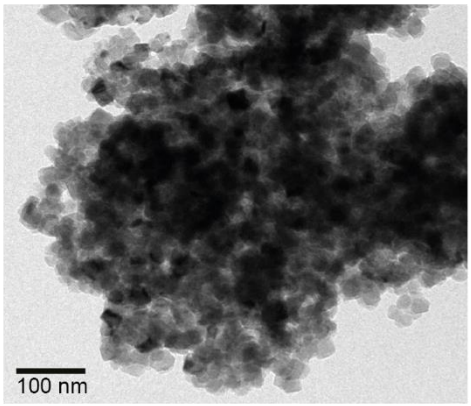

Fig. S2. Bright-field TEM image of PTI crystals obtained after one synthesis cycle of 2 days.

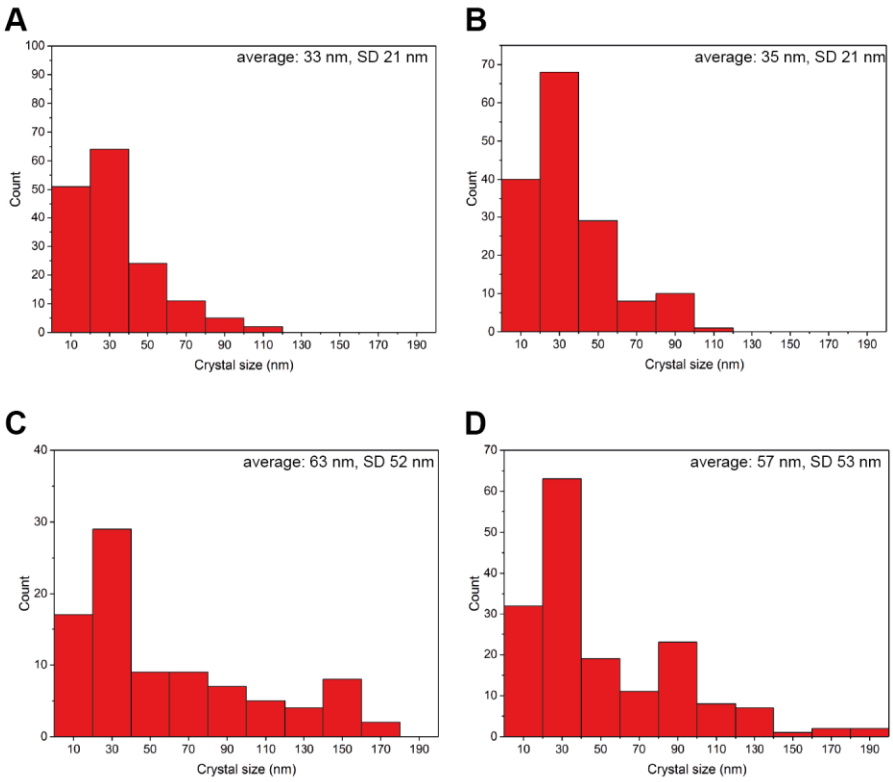

Fig. S3. PTI crystal size evolution with synthesis time. PTI crystal size histogram for a synthesis time of (**A**) 30 hours, (**B**) 2 days, (**C**) 6 days, and (**D**) 30 days. In all the cases the precursor amount was the same: 500 mg of melamine.

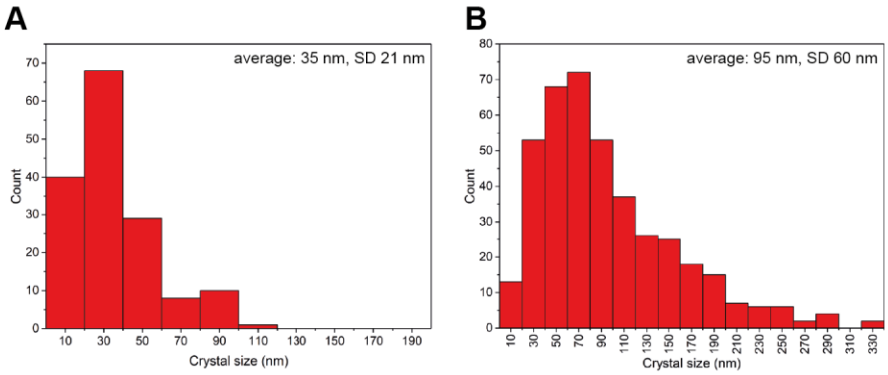

Fig. S4. PTI crystal size evolution with number of synthesis cycles. (**A**) PTI crystal size histogram for one synthesis cycle of 2 days using 500 mg of melamine as precursor. (**B**) PTI crystal size histogram for two synthesis cycles. The first one of 2 days using 500 mg of melamine as precursor and the second one for 6 days using a mixture of 500 mg of melamine and 100 mg of PTI crystals from the first cycle as precursor.

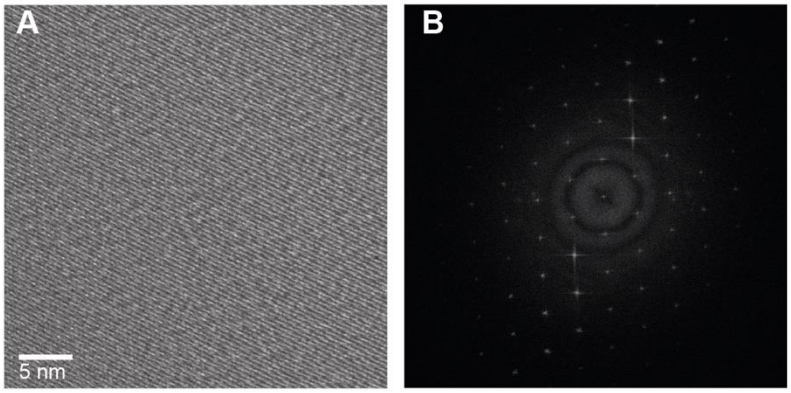

Fig. S5. HRTEM of PTI platelets. (**A**) HRTEM image of a PTI crystal obtained after two synthesis cycles of two and six days. (**B**) Corresponding FFT image.

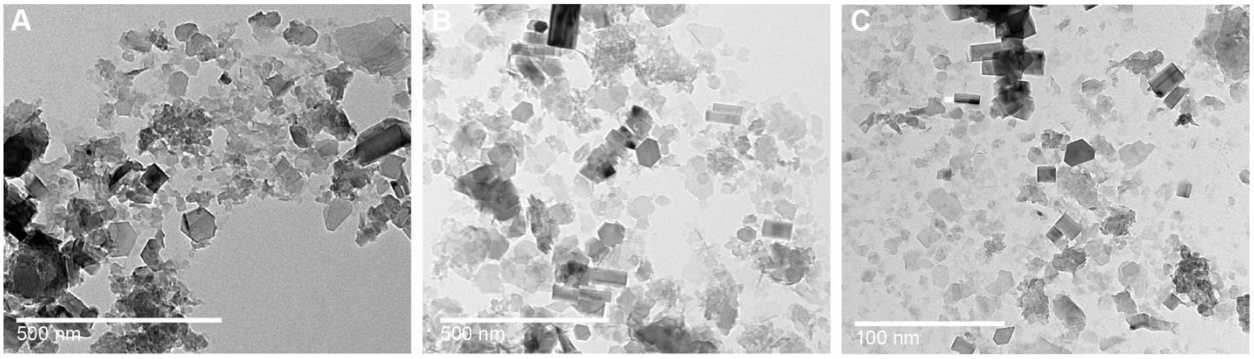

Fig. S6. Evolution of the exfoliation of PTI in anhydrous DMAc at 100°C. Bright-field TEM images from the solution after stirring for (**A**) 6 hours, (**B**) 12 hours and (**C**) 2 days. It was possible to observe exfoliated nanosheets even after 6 hours.

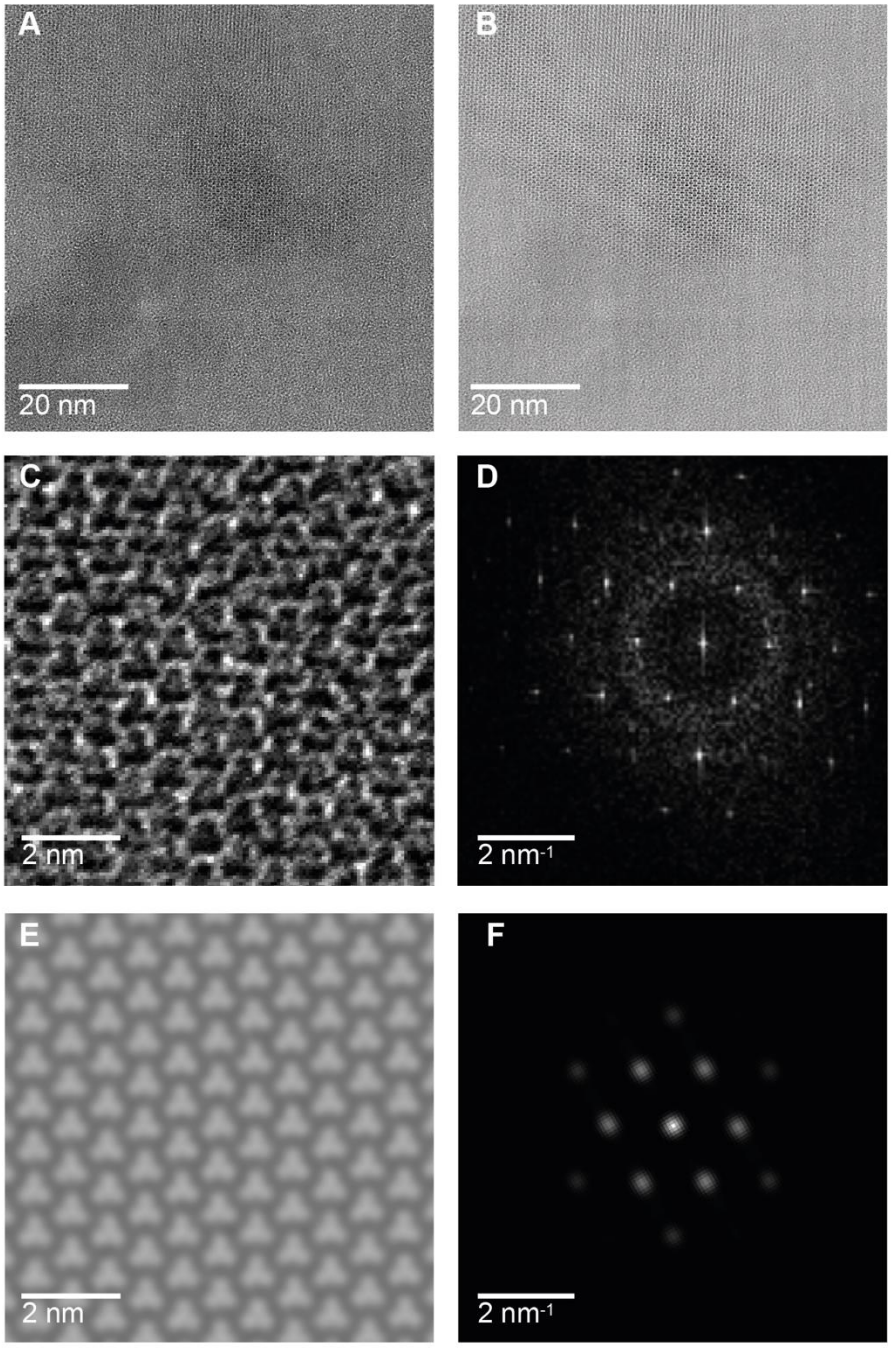

Fig. S7. HRTEM images of a single-layer PTI nanosheet. (**A**) HRTEM image of a single-layer PTI nanosheet and (**B**) its corresponding filtered image. (**C**) Zoom of the image shown in panel a) to show the triangular pores and (**D**) its corresponding FFT image. (**E**) Simulated HRTEM image of single-layer PTI using JEMS (Java Electron Microscopy Software). The input parameters correspond to the ones used to take the image shown in panel (A). (**F**) FFT image of the simulated HRTEM image of single-layer PTI.

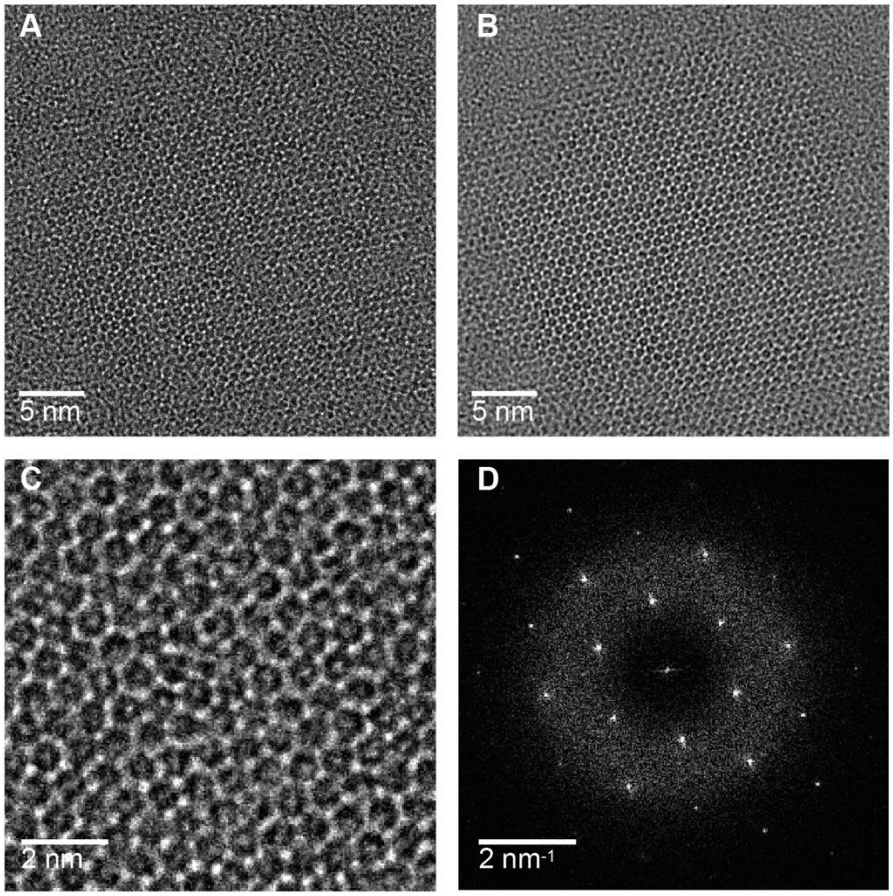

Fig. S8. HRTEM images of a few-layer PTI nanosheet. (**A**) HRTEM image of a few-layer PTI nanosheet and (**B**) its corresponding filtered image. (**C**) Zoom of the image shown in panel a) to show the hexagonal pores and (**D**) its corresponding FFT image.

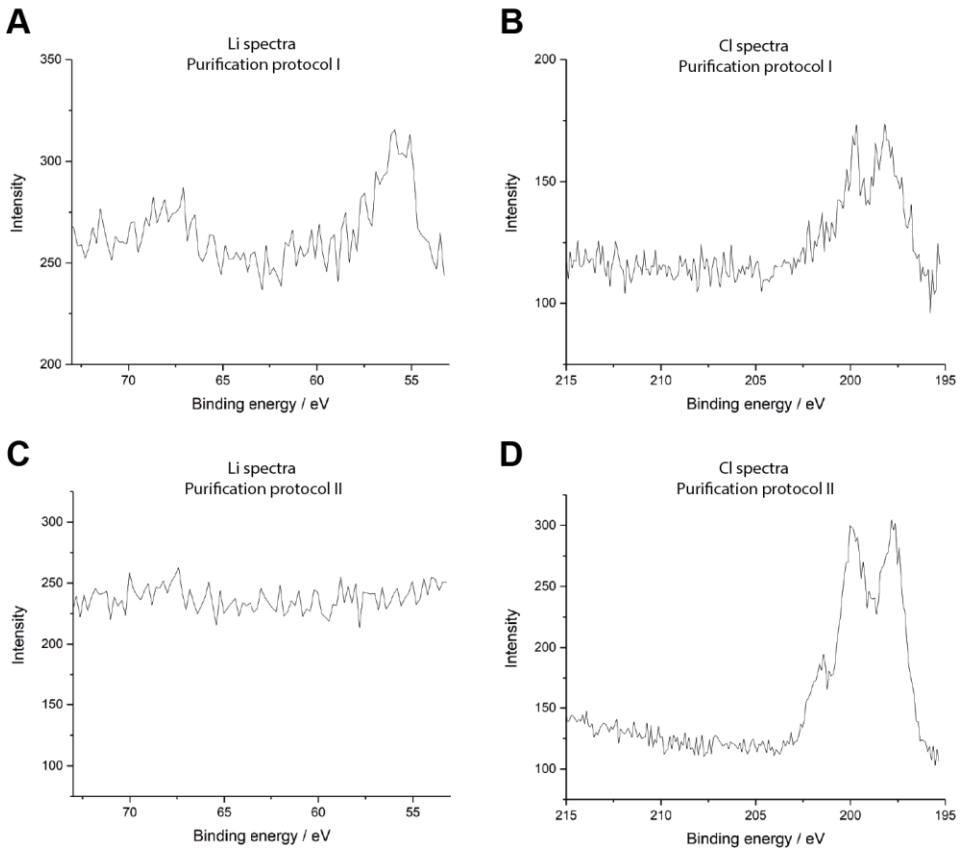

Fig. S9. XPS spectra of PTI nanosheets. (**A**) Li and (**B**) Cl spectra of PTI nanosheets purified using 3 centrifugation steps of 10 minutes each at 5000, 10000, and 15000 g respectively (purification protocol I). (**C**) Li and (**D**) Cl spectra of PTI nanosheets purified using a similar procedure but doing the last step at 15000 g for 3 hours instead to obtain predominantly single-layer PTI nanosheets (purification protocol II).

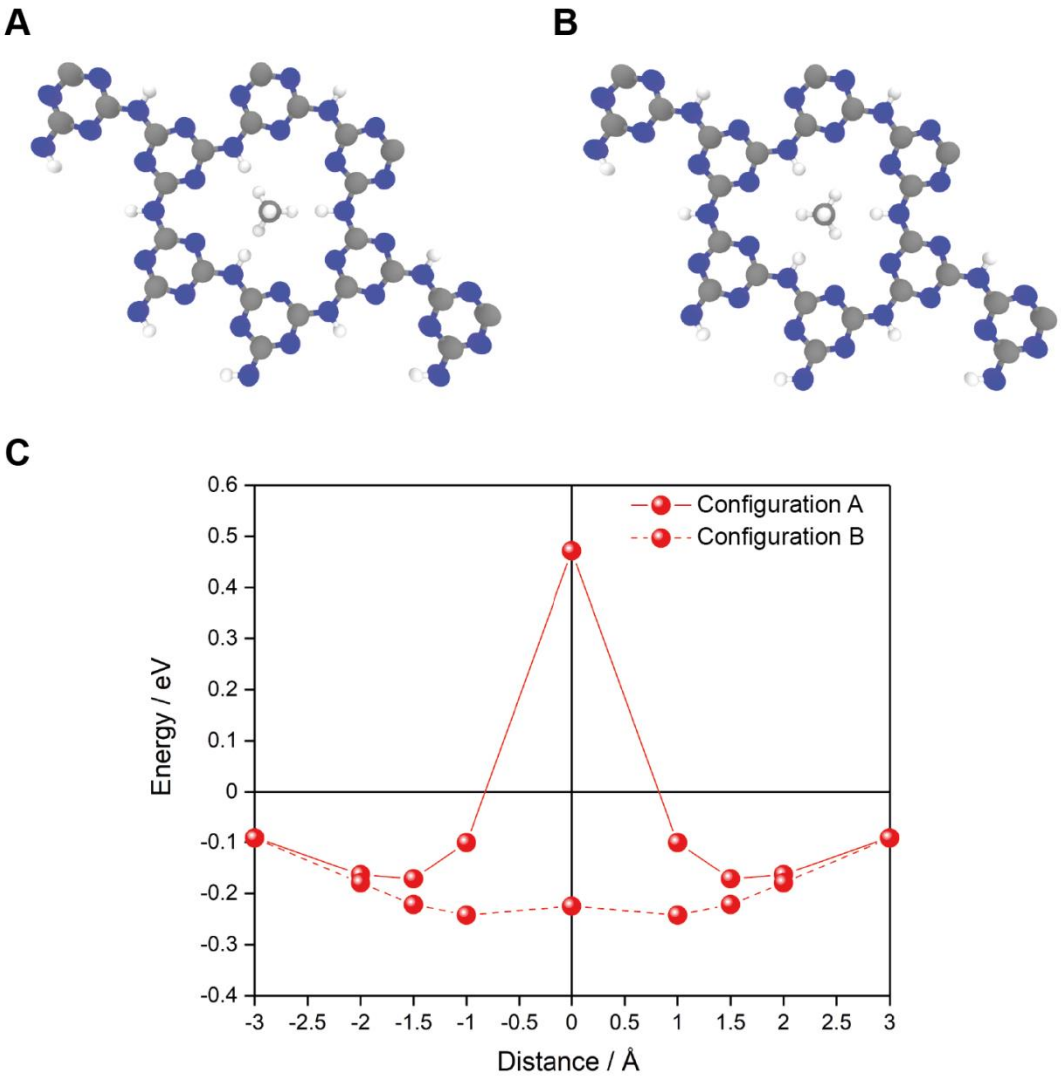

Fig. S10. Interaction of methane molecule with PTI single-layer nanosheet. (**A**) Configuration of methane molecule with its hydrogen atoms aligned with the hydrogen atoms at the edge of the pore of the PTI nanosheet. (**B**) Configuration where the hydrogen atoms of methane are as far as possible from the hydrogen atoms at the edge of the pore of the PTI nanosheet. (**C**) PES profile of methane on a PTI monolayer at the two configurations shown in panel a and b.

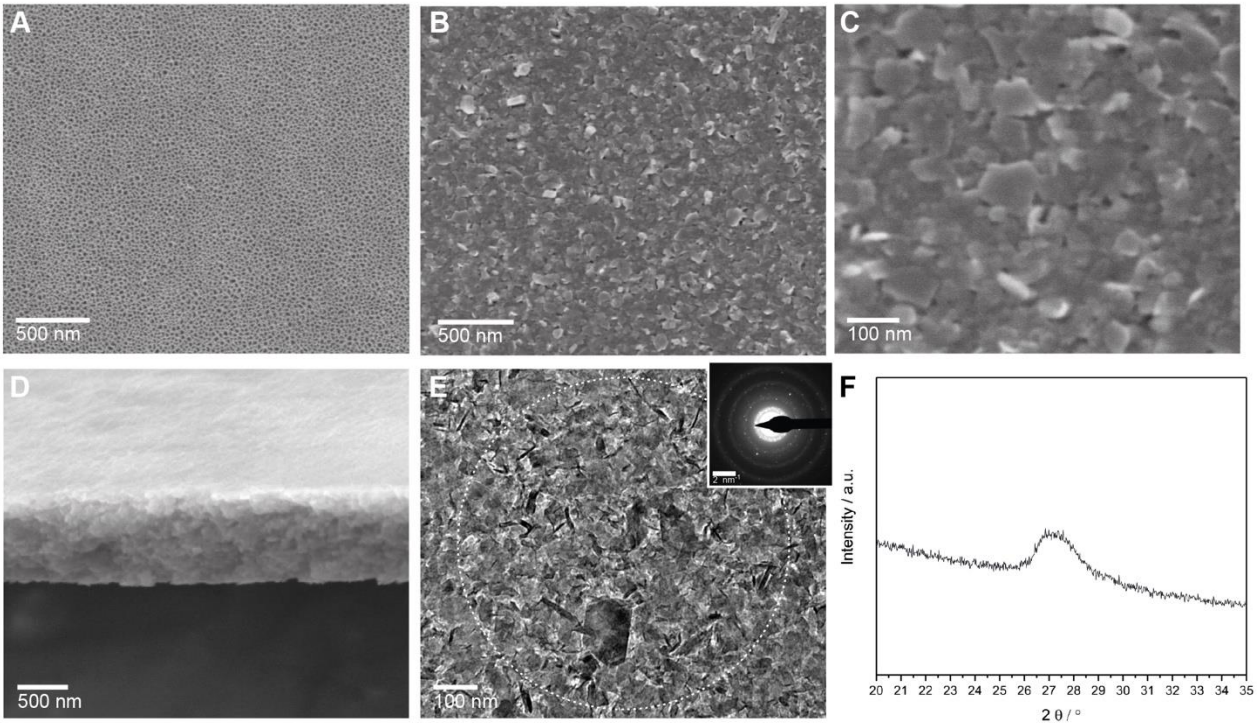

Fig. S11. Fabrication of gas-sieving PTI films via vacuum filtration. SEM images of the Anopore support before (**A**) and after (**B**) depositing the PTI nanosheets. (**C**) High magnification SEM image of the surface of the PTI film. (**D**) Cross section SEM of an isolated PTI film. (**E**) Bright-field TEM image of an isolated PTI film. Inset shows the SAED of the marked area. Bright-field TEM imaging of a free-standing film did not reveal any obvious packing defects, while SAED confirmed that the nanosheets in the packed film were crystalline. (**F**) XRD pattern of the isolated PTI film formed by the assembly of PTI nanosheets. The broad peak at 26.3-28.3° corresponds to an interlayer *d*-spacing of 0.32-0.34 nm.

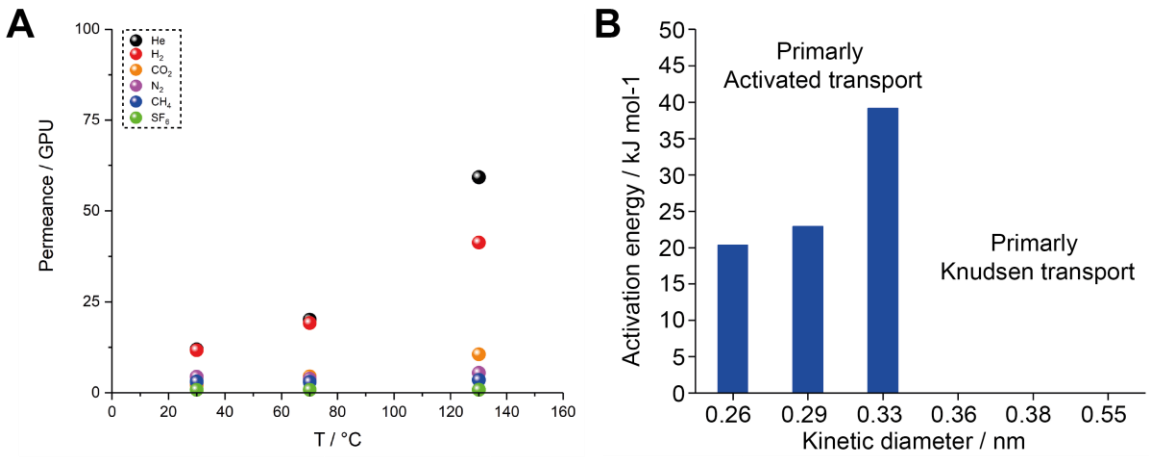

Fig. S12. Gas permeation data for PTI membranes. (**A**) Gas permeance for 6 different gases as a function of temperature from a pure PTI film. (**B**) Activation energies for gases as a function of kinetic diameter from a PTI film. See supplementary note III for details on the calculation of the activation energies.

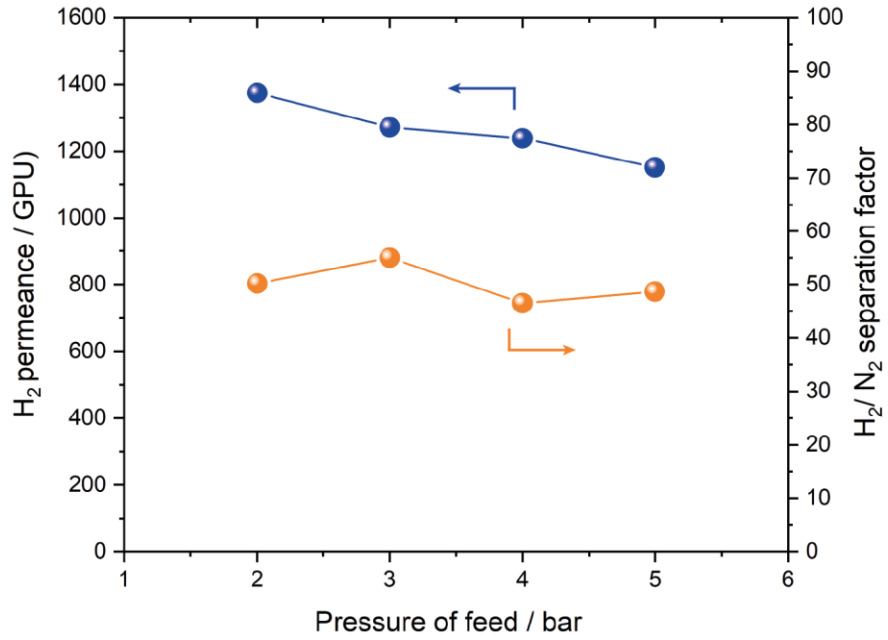

Fig. S13. Mixed-gas performance of the PTI membranes with *m*-PBI chains as spacers between PTI nanosheets at 250°C. H_2 permeance and H_2/N_2 separation factor as a function of the pressure used in the feed side for a feed composition of 50:50 H_2:N_2 and a temperature of 250 °C.

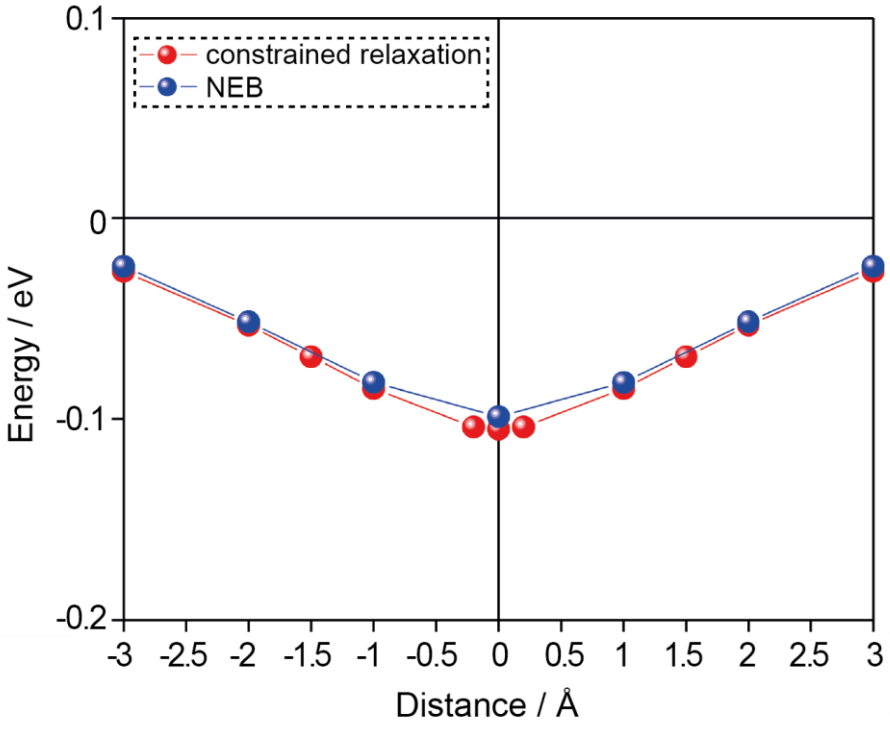

Fig. S14. PES for H_2 on a PTI monolayer calculated using the NEB and the constrained relaxation methods.

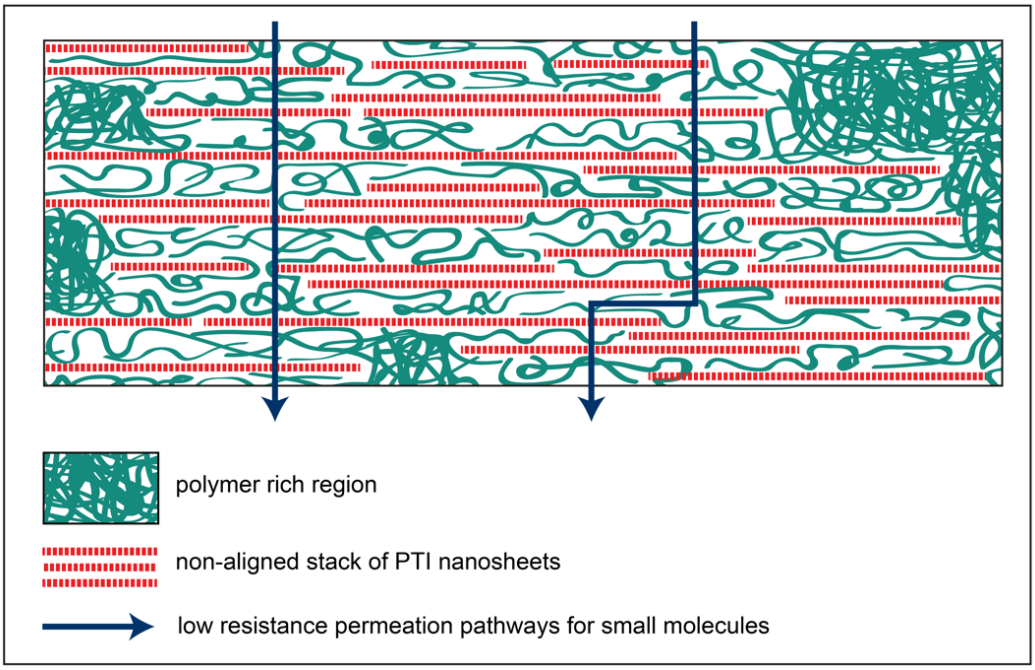

Fig. S15. Diagram showing the selective layer of PTI membranes with *m*-PBI chains as spacers. The diagram shows three possible arrangements in the selective layer (i.e., polymer rich regions, non-aligned stacks of PTI nanosheets, and low resistance permeation pathways formed when few m-PBI chains separate PTI nanosheets).

Table S1. Elemental analysis of PTI crystals using different synthesis conditions.

Sample	C (wt%)	N (wt%)	H (wt%)	C/N/H	C/N	H/N
Synthesized inside quartz ampule under vacuum	28.65	50.50	1.27	$C_3N_{4.5}H_{1.6}$	0.66	0.35
Open crucible: One synthesis cycle (2 days)	28.92	50.75	1.64	$C_3N_{4.5}H_2$	0.66	0.45
Open crucible: Two synthesis cycles (2 days and 6 days)	28.95	52.10	1.28	$C_3N_{4.6}H_{1.6}$	0.65	0.34
Theoretical composition of PTI	29.59	51.76	1.24	$C_3N_{4.5}H_{1.5}$	0.67	0.34

Table S2. Li and Cl content on PTI nanosheets. The analysis was carried out using the XPS data shown in fig. S9. We note that the preparation type I was used to fabricate membranes by self-assembly.

Purification protocol for exfoliated nanosheets	Type of nanosheet	Li content (atomic %)	Cl content (atomic %)
Not applicable	As-synthesized PTI crystals	5	5
I	Exfoliated. Centrifugation protocol as following: 5000 g for 10 min, 10000 g for 10 min, 15000 g for 10 min	2.8	0.2
II	Exfoliated. Centrifugation protocol as following: 5000 g for 10 min, 10000 g for 10 min, 15000 g for 3 hours	below detection limit	0.5

Table S3. Performance of PTI nanosheet films incorporating *m*-PBI chains at different temperatures. Data for three membranes is presented. Sample M1 was sealed using GC potting epoxy and could be tested safely up to 150 °C. Sample M2 and M3 were sealed with high temperature resistance epoxy.

Membrane and temperature	Permeance / GPU				
	He (2.6 Å)	H_2 (2.89 Å)	CO_2 (3.3 Å)	N_2 (3.64 Å)	CH_4 (3.8 Å)
M1 at 250 °C	-	-	-	-	-
M2 at 250 °C	761	922	88	19	12
M3 at 250 °C	1200	1448	150	31	25
Average at 250 °C	980	1185	119	25	19
M1 at 200 °C	-	-	-	-	-
M2 at 200 °C	402	517	55	10	8
M3 at 200 °C	718	871	85	18	14
Average at 200 °C	560	694	70	14	11
M1 at 150 °C	299	317	43	3	6
M2 at 150 °C	264	289	22	5	1
M3 at 150 °C	416	517	52	8	9
Average at 150 °C	326	374	39	5	5
M1 at 100 °C	130	129	14	1	1
M2 at 100 °C	126	131	10	2	1
M3 at 100 °C	229	277	38	6	6
Average at 100 °C	162	179	21	3	3
M1 at 30 °C	31	28	3	-	-
M2 at 30 °C	-	-	-	-	-
M3 at 30 °C	87	90	11	-	-
Average at 30 °C	59	59	7	-	-

Supplementary Note I. Carbon nitride membranes fabricated using polymeric melon

Several reports claiming the synthesis and exfoliation of g-C_3N_4 actually dealt with polymeric melon with intralayer hydrogen bonding. This was clarified in a recent review paper that reported the misleading classification of many poly-heptazines as g-C_3N_4.(*37*) Simple pyrolysis of carbon nitride precursors will form a polymeric carbon nitride, referred to as melon, and not the expected graphitic structure. Any exfoliation attempt that disrupts the π-π stacking between the layers of polymeric melon with intralayer hydrogen bonding is also expected to break the hydrogen bonds within the layer, leading to amorphous structure. As a result, even though, synthesis of membranes based on polymeric melon has been recently demonstrated,(*10*, *54*) size-sieving performance for gas molecules and ions in line with the triangular electron-density gap of g-C_3N_4 pores has not been reported. This can be achieved by synthesizing and exfoliating crystalline PTI which is one of the few carbon nitride materials with strong intralayer covalent bonds, making exfoliation of high-quality sheets possible.

Supplementary Note II. Ab initio simulation of interaction between CH_4 and a PTI nanosheet

For methane molecules, geometry optimization during the calculations is extremely important because it has a tetrahedral molecular geometry. CH_4 needs to overcome a large energy barrier when its hydrogen atoms are aligned with the hydrogen atoms at the edge of the pore of the PTI nanosheet (Fig. S10A). On the other hand, it is easily adsorbed when it rotates 60 ° to avoid the hydrogen atoms from PTI (fig. S10B). Fig. S10C shows the PES profile for these two configurations of methane. It is evident that methane molecules can cross PTI nanopore in only a few of all its possible configurations.

Supplementary Note III. Calculation of activation energy

The permeance of gas molecules through the nanopores of PTI in the assembled membranes can be related to the activation energy for transport if the transport is temperature activated (Equation 4)

$$Gas\ permeance \propto Ae^{\left(-\frac{E_{act}+E_{sur}}{RT}\right)} \quad (4)$$

where A is the pre-exponential factor, E_{act} is the activation energy to translocate the pores, E_{sur} is the energy of adsorption on the PTI pore, R is the universal gas constant, and T is the operation temperature. By linear fitting of *ln*(permeance) and 1/T, the apparent activation energy $E_{app} = E_{act} + E_{sur}$ can be obtained. Based on the ab-initio simulations performed $E_{He,sur}$= -4 kJ/mol, $E_{H_2,sur}$= -10 kJ/mol, and

$E_{CO_2,sur}$= -23 kJ/mol. The E_{act} for each of the gases can be calculated by the equation $E_{act} = E_{app} - E_{sur}$.

Supplementary Note IV. Availability of pores of PTI nanosheets for transport of molecules

The gas permeance from self-assembled PTI films was lower than expected from films made with nanosheets containing >50% porosity. Ab-initio calculations show that small gases like He and H_2 can freely transport across single-layer PTI sheets. The observed low permeance is likely due to the low amount of interconnected pore channels, in the packed film, that are large enough to allow the transport of gas molecules. PTI nanosheets pack very well with an interlayer spacing that is too small (d-spacing of 0.32-0.34 nm, fig. S11F) to allow molecules to transport through the gaps between the sheets. Any misalignment in the stacking of the nanosheets will cause the partial or complete blocking of transport channels. Moreover, ions retained in PTI nanosheets, particularly in bi-layer and few-layer nanosheets, can block the transport pathways. A 900 nm thick PTI film is formed by stacking more than 2500 PTI nanosheets, and it takes only a few multilayer PTI nanosheets hosting ions or a few heavily misaligned nanosheets to block transport pathways.

Supplementary Note V. Use of *m*-PBI chains as spacers

Adding a small amount of m-PBI (ca. 0.06 mg/ml) to the dispersion of PTI nanosheets did not cause agglomeration of the nanosheets which motivated us to try to assemble them to form a composite structure in which m-PBI chains act as a spacer to the packing of PTI nanosheets. PBI can withstand harsh operation conditions and the interaction between m-PBI and PTI is expected to be good since both of them have functional groups capable of hydrogen bonding and both of them interact strongly with DMAc. The resulting membranes, fabricated by filtering 15 ml of a solution containing ca. 0.06 mg/ml of m-PBI and ca. 0.01 mg/ml of PTI nanosheets, were defect-free and yielded a good performance (Fig. 3, and S13). A conservative PTI loading (wt%) in the final membranes of 16 % was calculated assuming all the m-PBI molecules are retained during the filtration.

We hypothesize three packing scenarios between the PTI nanosheets and the m-PBI chains (fig. S15). In scenario 1, nanosheets are spaced apart with m-PBI chains. The membrane may contain phase-separated regions composed of a nanosheet rich phase where there is a stack of nanosheets without the polymer chains (scenario 2) or a polymer-rich phase without nanosheets (scenario 3).

We think that the arrangement and free-volume of m-PBI chains trapped between nanosheets is different than the bulk m-PBI film, which might have increased the transport of He and H_2 through the free-volume of trapped m-PBI chains. PTI nanosheets are expected to interact favorably with m-PBI chains via H-bonding (N-H is present in both of them) and π-π stacking (benzene from m-PBI and triazine from PTI). Moreover, the most stable interaction between triazine and benzene rings is when they are parallel one on top of the other. (55,56) Such interactions can guide the m-PBI polymer chains to the surface of the PTI nanosheets, disrupting the packing of m-PBI chains that is observed in the bulk.

Overall, the separation performance of the hybrid PTI/m-PBI selective layer is dominated by the interconnected highly permeable regions where the PTI nanosheets are spaced apart by m-PBI chains. It is likely that the m-PBI spacer between the nanosheets possess higher free volume than that in the bulk m-PBI phase. Therefore, small molecules like He and H_2 have enough space, thanks to the m-PBI spacer, to move and find a nanopore in the subsequent nanosheet to continue crossing the selective layer. On the other hand, the larger molecules that require a very high activation energy to translocate PTI, have to go through the low-permeability m-PBI rich phase.